

Research Article

Effect of Surface Hardening on Dynamic Frictional Rolling Contact Behavior and Degradation of Corrugated Rail

Yuan Gao ^{1,2}, Jingmang Xu ^{1,2}, Ping Wang ^{1,2} and Yibin Liu^{1,2}

¹MOE Key Laboratory of High-Speed Railway Engineering, Southwest Jiaotong University, Chengdu 610031, China

²School of Civil Engineering, Southwest Jiaotong University, Chengdu 610031, Sichuan, China

Correspondence should be addressed to Jingmang Xu; mang080887@163.com

Received 25 April 2019; Revised 7 July 2019; Accepted 28 July 2019; Published 25 August 2019

Academic Editor: Mario Terzo

Copyright © 2019 Yuan Gao et al. This is an open access article distributed under the Creative Commons Attribution License, which permits unrestricted use, distribution, and reproduction in any medium, provided the original work is properly cited.

The present study was undertaken to evaluate the effect of surface hardening technology on dynamic frictional rolling contact behavior and degradation of corrugated rail in Shenzhen. Characteristic parameters such as length and depth of corrugation were analyzed by means of a continuous measurement method based on the corrugation analysis trolley. The explicit finite element method for material hardening characteristics and real contact geometry was adopted to set up the 3D transient FE model of wheel and rail, after which the value and distribution of stress/strain as well as contact solutions could be obtained during frictional contact, and then the Archard wear model and simplified wear superposition method are integrated as a numerical simulation tool for rail wear after hardening. The simulation results show that laminar plasma surface hardening technology can increase residual stress and shear stress in quenched zones, leading to local stress concentration at their boundaries; the plastic strain in the matrix material is higher than that in the quenched zones, while the strain concentration is mainly focused on the matrix material. The hardening can remarkably reduce the rail wear along the corrugation wave, and the wear depth of material with hardening technology is about 36% of that of nonhardening material. Laminar plasma surface hardening technology can therefore restrain the development of rail corrugation.

1. Introduction

Since Shenzhen Metro Line 11 went into operation, short-wavelength corrugation has been discovered on the surface of metro rails after two years in service. When in contact with a corrugated rail, the wheel resonates at its surface, and the resonant vibration may occur within an inherent frequency range, causing a high-frequency rail vibration and worsening wheel-rail damage, leading to higher frequency vibrations along the rail and degradation of fastener during operation (for example, between January and March 2017, elastic bar cracks were discovered at 103 points, with 6 elastic bars broken down and 12 anchor bolts fractured). Moreover, rail corrugation poses a serious threat to the safety of trains [1, 2]. At the moment, rail grinding can effectively mitigate rail corrugation, but frequent grinding significantly increases the cost of rail maintenance. To effectively control and mitigate short-wavelength corrugation, the surface

hardening technique can be used as an effective way to increase the service life of rail.

Figure 1 shows the rail treated with the laminar plasma hardening technique using laminar plasma jet. The laminar plasma hardening technique requires a digitally controlled bundle-like ultrahigh-temperature heat source (whose temperature can accurately be selected between 500 and 15,000°C) to rapidly heat a rail with energetic plasma so that its surface temperature can quickly rise over the critical phase transition point yet remain below its melting point. A quick cooling of the rail then takes place; due to its good thermal conductivity, martensite with high hardness and wear resistance is formed, with the significant increase in local hardness and residual compressive stress, while leaving the internal structure and performance unchanged. After heating, an ultrafine and homogeneous hardened structure form at the rail surface. In addition, due to the low depth of the laminar plasma quenching layer (0.4 mm–1.5 mm) and

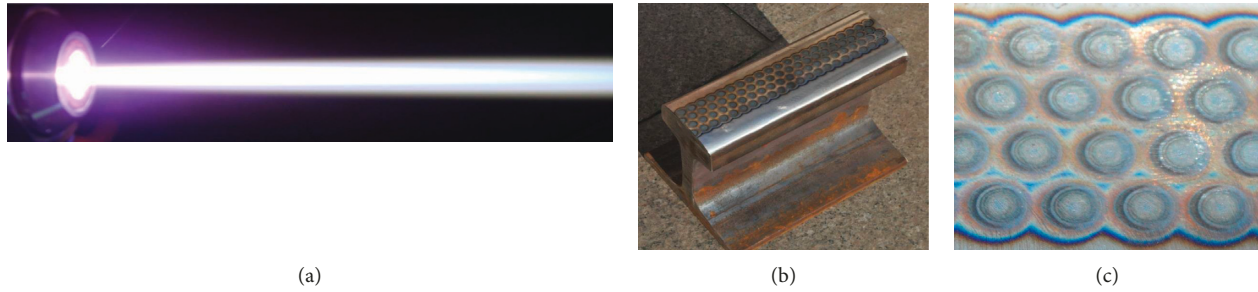


FIGURE 1: The laminar plasma hardening technique: (a) laminar plasma jet; (b) rail treated with the laminar plasma hardening technique; (c) close-up of laminar plasma hardening rail.

the controllability of the quenched zone (which can accurately be adjusted between 1% and 100%), the hardening structure, as well as the surface martensite, has little impact on the bearing characteristics of the structure. Safety can thus be guaranteed, meaning the laminar plasma hardening technique is a new method suitable to prevent metro rail corrugation from worsening.

To date, in order to prevent the development of rail corrugation, many studies have been carried out on the cause and growth of rail corrugation by means of simulation or experiment method. Grassie [3] analyzed and summarized the characteristics, causes, and solutions of various rail corrugations by means of experiment, concluding that corrugated rails are corresponding to the problem of fixed frequency. Torstensson and Schilke [4] investigated the development of corrugated rail and noise vibration level of Swedish metro when the vehicles passed through the low rail in sharp curves at a speed of 30 km/h, and then a numerical tool is used for the prediction of rail corrugation growth on curves. Daniel et al. [5] established the nonlinear time-domain model of a bogie to investigate the rail corrugation; the model was tuned to match FE predictions of its natural frequencies, the parameters were obtained from field experiment, and the model could predict the wavelength per sleeper of corrugation below 100 mm. Nielsen [6] predicted the growth of railhead roughness through numerical simulation of dynamic train-track interaction on tangent track, and the wheel-rail contact forces, creepage, and wear were calculated in relation to location along a discretely supported track model. Vila et al. [7] presented a model for calculating the wear located on the running surface of rail, and then the evolution of rail corrugation was investigated according to the cyclic track model after thousands of wheelset passages. Ling et al. [8] researched the effects of rail corrugation on dynamic performance of metro rail fastenings according to the extensive on-site experiments conducted and simulations of MBD dynamics; from the results of field experiments and dynamic simulations, the root causes of the clips fracture were recognized, and the suggestions for mitigating strong vibrations and failure of metro rail fastening systems were also made. Jin et al. [9] used the numerical tool hunting for the effect of sleeper pitch on the rail corrugation initiation and development at tangent track, considering the combination of Kalker's rolling contact theory, linear frictional work model, and dynamic model of a vehicle coupled

with the tangent track, and then the excited resonant frequencies of wheelset and track were calculated in detail at different running speeds. The necessary conditions for the occurrence of rail corrugation were given. Baeza et al. [10] presented a rotating flexible wheelset coupled with a flexible track model for investigating the rail corrugation growth, and the flexible model could simulate the vehicle-track interaction at high frequencies compared to the MBD method. Thus far, extensive research has been carried out on the initiation and growth of rail corrugation; however, there has been no complete theoretical explanation for the formation mechanism of corrugation, and no satisfactory solution to the problem has efficiently been proposed according to the experiment results. In order to prevent the development of corrugation, various models are established to analyze the dynamic behavior of interaction between wheel and corrugated rail, and many methods have been put forward to prolong the service life of rail, which have resulted in surface hardening technique being gradually applied in the railway industry. With the development of high-speed and heavy-load railway, more and more attention is paid to prolong the service life of rails. Surface hardening technique is an effective method of enhancing the wear resistance of the surface and guaranteeing proper wheel-rail relationship. The US Department of Transportation [11] carried out an evaluation of laser-hardened rails around 2005, indicating that laser hardening could permanently lower wheel-rail friction and prolong the service life of rails. However, considering that fatigue failure induced by laser hardening was difficult to solve, fatigue cracks often appeared in rails under wheel loading. Zheng et al. [12] calculated the service life of rails covered with different hardening areas by simulating laser hardening on the rail surface, investigated the wear resistance and contact fatigue resistance of the rails under different hardening schemes, and demonstrated the contact fatigue behavior of laser-hardened rails under loading. Cao et al. [13] researched the microstructure, wear, and rolling contact fatigue (RCF) characteristics of laser-hardened wheel-rail materials, and then the optimal laser hardening parameters suitable for wheel-rail materials were defined. Moreover, the RCF life of the rails is twice that of the matrix material under optimal laser hardening parameters. Zeng and Lu [14] analyzed the effects of hardening on the wear rate and RCF life of wheel steel using the Amsler double-disc tester, and then the test

results between the hardened and unhardened material were evaluated and compared. Shariff et al. [15] used laser hardening (without melting) and laser melting (surface melting) for rail surface processing and carried out a comparative analysis of the effects of laser surface hardening on the sliding wear performance of pearlitic rail steel.

Therefore, the surface hardening technique has gradually been introduced in rail processing, though there still remains a distinct lack of research into the mechanics mechanism caused on a hardened rail under wheel loading. According to the characteristics of a hardened rail, it is thus important to research the effects of surface hardening on stress/strain distribution regularities of rail and axle box vibrations using an explicit finite element model (FE model). The transient frictional rolling contact solutions, axle box acceleration, and the stress/strain during impact are investigated. This should help reveal the inhibitory action of the laminar plasma hardening technique on the development of rail corrugation so as to provide theoretical support for its application to metro rail processing.

2. Simulation and Experimental Procedure

To explore the effect of the surface hardening technique on the stress mechanism of corrugated rails and axle box acceleration, this paper tries to simulate wheel-rail interactions using an explicit finite element method (FEM) based on the central difference algorithm, introducing rail corrugation by means of a self-programmed application. An implicit-explicit method was then used to develop a solution for wheel-rail transient contact and calculate stress mechanism of corrugated rails and axle box acceleration under wheel loading. The schematic logic is shown in Figure 2.

To explore the stress regularities and damage characteristics of corrugated rails after surface hardening, the structure and schematic logic of the paper is shown in Figure 2. First, the feature sizes of rail corrugation in typical metro areas are tested, including wavelength and depth of convolution. Then, considering the actual wheel-rail contact geometry and flexibility in metro rails, a 3D FE model was built for predicting degradation and vibration characteristics of corrugated rail using finite element software. According to the principle of hardening, the FE model is established based on the properties of a hardened material and rail matrix material [12]. Rail corrugation can be simulated by changing the 3D coordinates of the nodes in the FE model. Then, the central difference method is applied to calculate solutions for wheel-rail interactions, and this includes wheel-rail forces, rail stress-strain, and axle box acceleration. Based on the Archard wear model and transient rolling contact solutions, the longitudinal distribution regularity of wear is calculated to reveal the impact of hardening on the stress mechanism and vibration characteristics of rails under wheel loading, and then, the inhibitory action of hardening on the deterioration of rail corrugation is evaluated. It has been proven in the existing literature [16] that an explicit dynamic model can be used to analyze the dynamic wheel-rail interaction. In addition, the finite element method can consider different material models and accurately calculate

the wheel-rail frictional contact solutions and rail wear, with full consideration given to the effects of hardening materials on the stress mechanism and vibration characteristics of the wheel and rail.

2.1. Measurement of Rail with Wave Corrugation. There are two methods for rail corrugation measurement: the indirect method of measurement can be used to measure the indirect indexes (noise, rail, or axle box vibrations) under wheel-rail contact to calculate the wavelength and depth of rail corrugation. This method can define characteristic parameters for corrugation based on vibration or abnormal noise, especially at the stage of corrugation initiation, but it is susceptible to the driving environment and the irregularities of the rail surface. The direct method can directly measure the characteristic parameters of corrugation using a sensor on the rail surface, and the measurement results are visual and highly accurate, which can directly reveal characteristic parameters of corrugation, including depth and wavelength. With the development of rail corrugation measurement technology and computer storage technology in recent years, it is possible to measure rail corrugation to a great degree of accuracy and efficacy on a large scale. Therefore, the direct measurement method is adopted in this paper to measure the characteristic parameters of rail corrugation directly.

The characteristic parameters of the corrugated rail are measured by the corrugation inspection car (m|rail Trolley). The inertial reference method is applied to measure the corrugation, when the acceleration sensors are installed on the body of corrugation inspection car. According to the principle of inertia, if the vibration frequency of axle acceleration is much higher than the natural vibration frequency of the mass spring system including car body and axle box, the car body will be in a static state. Assuming the car body as a reference for measurement, the method is only suitable for measuring corrugation with short wavelength [17]. When the wheel remains in contact with the rail, the vertical displacement Z of the car body can be obtained based on the acceleration through quadratic integration from sensors installed on the car body. The relative motion W between car body reference and axle box can be obtained from the displacement sensor. For the collected vibration acceleration signal and displacement, the denoise processing is adopted to avoid the low-frequency interference effects caused by noise. The displacement H of the axle box is the depth of corrugation, which equals to the sum of Z and W , and the depth of corrugation along the longitudinal direction of the rail can be obtained. Then, the periodogram method is applied to obtain the power spectrum of corrugation, from which, the length of corrugation will be observed.

Focusing on Shenzhen Metro Line 11, this paper measures the characteristic parameters of corrugation such as depth and wavelength, according to the working principle of corrugation inspection car. Because the corrugation in metro is of short wavelength, the corrugation inspection car can get accurate measurement data. Figures 3 and 4 show the field test drawing and target corrugated rail in metro. The measurement covers

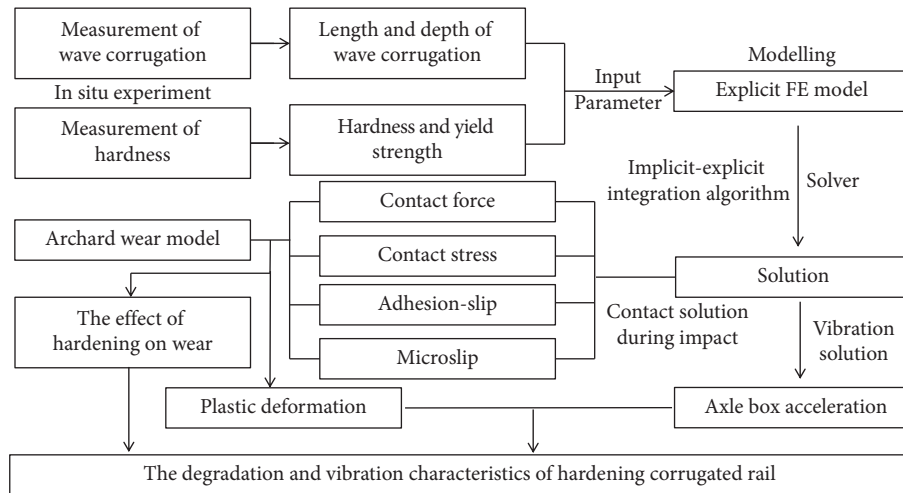


FIGURE 2: Structure and the schematic logic.



FIGURE 3: Measurement of rail with wave corrugation.



FIGURE 4: Rail with wave corrugation.

a distance of ZDK6 + 240 m~ZDK6 + 550 m with a serious problem of screaming of train and failure of fastener. The amount of fastener failure is about 30% of the total failures, and the serious corrugation was observed at the place where the elastic strip was broken. Wave depth and length can be observed from the measured rail irregularities and spectral power density function. The measured results of the short-wave irregularities on the rail surface and the spectral power density function for rail corrugation are shown in Figure 5.

As can be seen in Figure 5, there are two high crests in the figure of the short-wave irregularities on the rail surface. The two crests, 25 m apart, are triggered from rail welding joints and should be rejected during corrugation analysis. To calculate the wave depth in this section, a piece of software programmed in Matlab was used to look for wave crests and troughs in the curve. The average value of the vertical coordinate difference between many wave crests and troughs was then used for depth calculation. The true depth of rail corrugation is about 0.15 mm. The power spectral density function graph for rail corrugation is shown in Figure 6. There is an obvious crest value at the 80 mm wavelength in this section of the rail. This shows that, for the typical corrugated section of the measured metro rail, the wavelength should be equal to 80 mm. The corrugation in metro is the typical short-wave irregularity.

2.2. Modeling of Wheel and Rail with Wave Corrugation.

Rail 60 on Shenzhen Metro Line 11 was taken as the object for this study. Considering that hardening has effects on material performance and that there are some high-frequency contents in a wheel-rail impact excited by short-wavelength corrugation, in this paper, a wheel-rail impact on the hardened corrugated rail section is simulated using an explicit FEM in order to faithfully reveal the effects of hardening on the stress mechanism and vibration characteristics of the rail material.

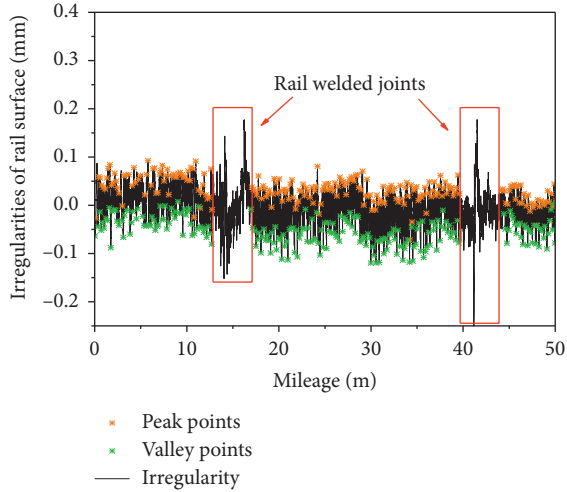


FIGURE 5: Irregularities on rails with short-wavelength corrugation.

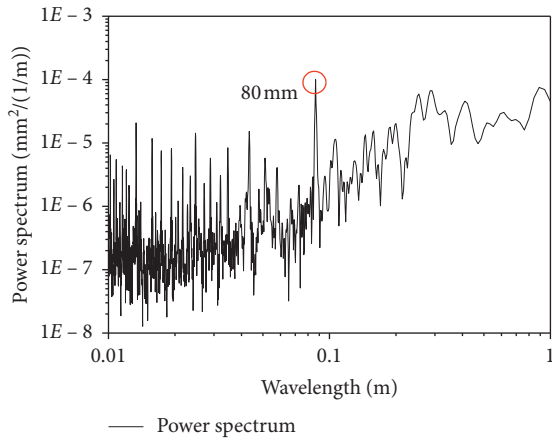


FIGURE 6: Power spectrum for rails with short-wavelength corrugation.

Figure 7 shows the schematic diagram of the FE model. The length of the finite element model is 15 m, which is enough to eliminate the boundary effects during simulation. The model consists primarily of real wheel, real rail, primary suspension, sprung mass, and rail pad. The wheel and rail are characterized by an 8-node solid element of SOLID164. The wheel profile is S1002, and the rail is a standard UIC60 rail, which is also modeled by the 8-node solid elements of SOLID164. In order to simulate the impact of surface hardening on wheel-rail interactions, the parameters are determined based on the selective laminar plasma quenching principle. The hardened patch size is shown in Figure 8 modeled by the 8-node solid elements of SOLID164. The hardened patch is semispherical, with a radius of 5 mm and depth of 0.8 mm. The distance between the centers of two hardened patches is 9.1 mm with the patches being evenly distributed along the railhead. To reveal the impact of hardening on the stress mechanism and vibration characteristics of the corrugated rail, the contact element mesh size in the contact zone and hardening patches was set to 0.4 mm, while the rest was discretized using transitional meshes, meaning the maximum mesh size in the model was 0.2 mm.

In order to consider the plastic deformation under wheel loading, bilinear elastoplastic materials were applied to the wheel and rail. The difference between matrix and hardening material can be reflected by yield stress and hardness [18–20, 22, 23]. To go into more detail, the constituent material of the wheel was ER0 rolled steel; the rail was mainly made of U75V steel, whose density, Young's modulus, yield strength, Poisson's ratio, and hardness are shown in Table 1, respectively. The coefficient of friction was set to 0.5, and friction between the wheel and rail were defined based on Coulomb's friction law, while wheel-rail interactions were simulated using a penalty function-based surface-to-surface contact algorithm. The detailed values of parameters used in the model are shown as Table 1.

Since dynamic wheel-rail response has a strong correlation with stiffness and damping of the rail pad, the rail pad and primary suspension can be simulated by linear springs and viscous dampers, which can be modeled by COMBI165. Then, the material of stiffness and damping are fed to COMBI165 to simulate the spring and viscous damper. To avoid hourglass effect caused by load concentration, multiple spring-viscous dampers were used to bear wheel loads. A rail pad consists of a uniform grid of 7×7 discretely distributed spring-damper pairs (7 transverse springs and 7 longitudinal springs), with a pad length of 0.06 m. The primary suspension and the components above it are assumed as lumped mass of MASS166, which is connected to the axle center through primary suspension modeled by the spring of COMBI165. The sprung mass was 8 t.

After meshing the model, the hardening material needs to be given to the elements in the quenched zone, while the corrugated rail can be obtained by modifying the node coordinates in the evaluation area. According to the parameters of corrugation (wavelength: 80 mm; depth: 0.15 mm) measured during the tests, the depth of corrugation is defined as a sine curve in the vertical direction (y), while the lateral is defined as a parabola in the horizontal direction (x). The node coordinates are then modified based on the following formulas, and the corrugation is introduced into the evaluation area:

$$d_1 = -0.5d_2 \left(1 - \sin \left[\frac{2\pi(x - x_c)}{L + (\pi/2)} \right] \right), \quad (1)$$

$$d = d_1 \left[1 - \left(\frac{y}{W} \right)^2 \right], \quad (2)$$

where d_2 , L , and W represent the maximum depth, wavelength, and width of rail corrugation, equaling 0.15 mm, 80 mm, and 30 mm, respectively; d_1 represents the maximum depth in the horizontal direction, located at the middle of the corrugation; and x_c represents the longitudinal coordinate of the starting point of corrugation, equaling 1.2 m.

Since the stress mechanism and degradation of the rails are directly related to the yield strength and hardness of the material, in order to consider the new material in hardened patches after surface hardening. Therefore, a bilinear kinematic reinforced material was used. After hardening, the yield strength and hardness of the rail material improved significantly. To be specific, the yield strength increased from

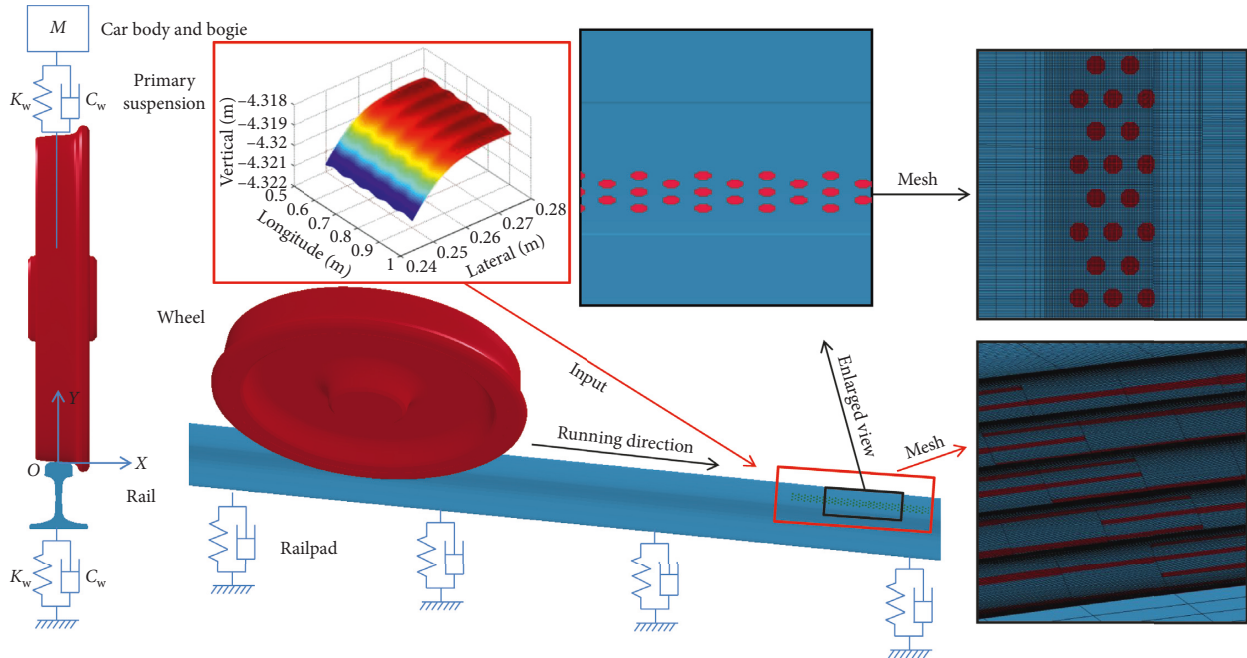


FIGURE 7: Schematic diagram of wheel-rail interaction with close-ups of mesh.

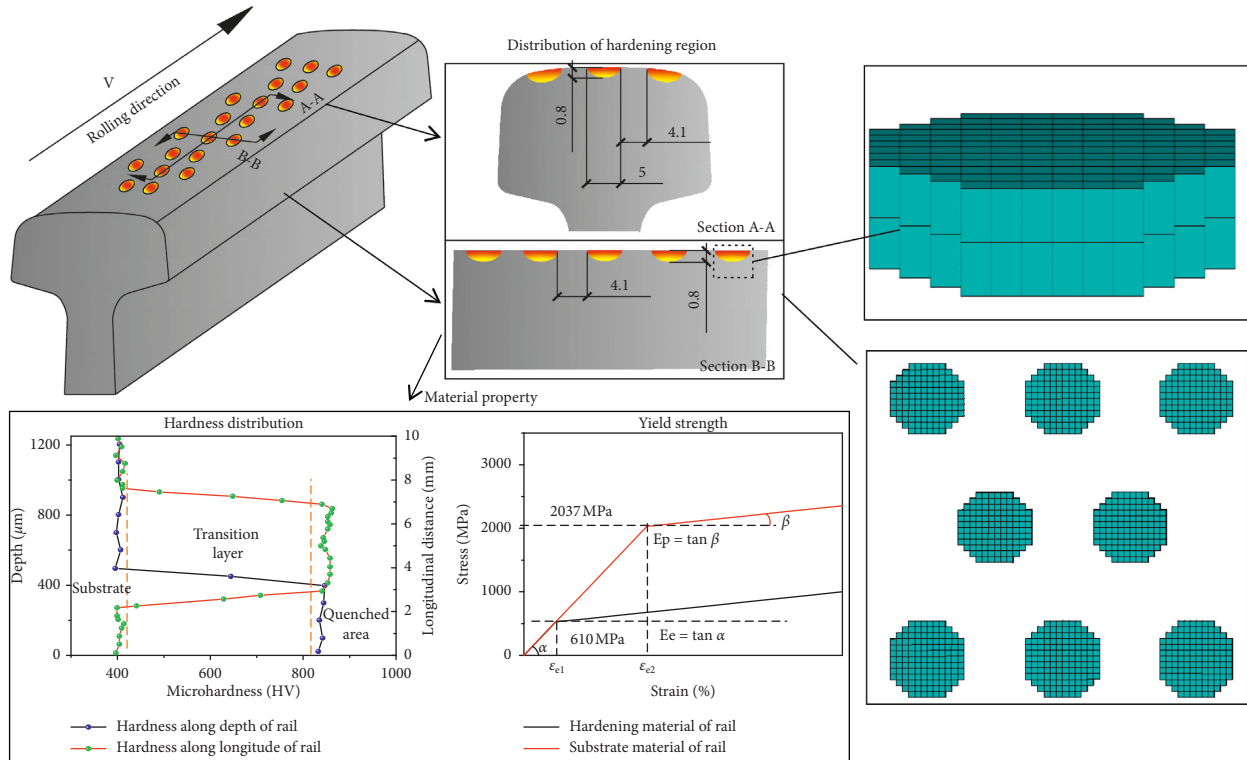


FIGURE 8: Schematic diagram of wheel-rail interaction with close-ups of mesh.

610 MPa to 2037 MPa, and the hardness increased from 400 HV to 820 HV (Figure 8). Due to a certain range of the transition layer between the quenched zone and the matrix material, the hardness and yield strength of this transition layer can be measured by linear interpolation.

After the FE model was set up, the implicit-explicit method can be used to solve wheel-rail contact. First of all, the system is put in its initial position to calculate the displacement field under static wheel-rail conditions (an implicit static solution). Then, the wheel-rail displacement

field under static loads is defined as the initial state of the explicit dynamic solution, while the rolling speed of the wheel and the forward velocity of the train are taken as the initial conditions. A torque load is prescribed on the axle to generate a longitudinal traction force, and the braking force generated by the torque accounts for 30% of static loads, with the inertia of the wheel ignored. The state of motion changes as the wheel begins to enter the dynamic state which leads to the initial excitation, meaning a section of some length is required to eliminate the dynamic excitation and enable the wheel to roll in an approximate steady state.

2.3. Verification of the Model. In the model, after the energy of dynamic excitation is consumed, the wheel can move in an approximately steady state. This guarantees the feasibility of solution verification for transient wheel-rail contact (Table 2).

The contact force between wheel and rail cannot be measured accurately by experimental methods. The solution of wheel-rail interaction is rarely verified directly especially under dynamic condition [21], so the indirect verification is proposed: the reliability of results can be verified by the contact solution in approximately steady state. The contact solution was verified at 0.02 s with CONTACT and Hertz, and the results of contact force and stress agree well. The model can simulate the interaction and vibration between wheels and rail precisely.

2.4. Prediction of Rail Degradation with Wave Corrugation. In order to reveal the impact of surface hardening on the damage of corrugated metro rails, this paper tries to make an evaluation of deformation and wear. Considering that plastic deformation is not an output variable of LS-DYNA, the magnitude and distribution of plastic deformation can qualitatively be described according to the numerical relationship between the von Mises stress and yield strength. In the light of the von Mises yield criterion, the deformation corresponding to the stress state at one point on the rail can reach its limit, meaning that this zone will start entering the plastic state, as follows:

$$\bar{\sigma} = \frac{1}{\sqrt{2}} \sqrt{(\sigma_x - \sigma_y)^2 + (\sigma_y - \sigma_z)^2 + (\sigma_z - \sigma_x)^2 + 6(\tau_{xy}^2 + \tau_{yz}^2 + \tau_{xz}^2)}, \quad (3)$$

where σ_x , σ_y , and σ_z represent the normal stress and τ_{xy} , τ_{yz} , and τ_{xz} represent the shear stress. To analyze the wear loss of hardened corrugated rails under wheel load, based on the contact solutions obtained from the FE model, an Archard sliding friction wear model is used based on the adhesive wear mechanism. The model assumes that the wear of the material only occurs in a sliding area rather than an adhesive area, meaning that wear loss in contact patches can be expressed as

$$V_w = \frac{k_w F_n d}{H}, \quad (4)$$

where V_w represents the wear volume of the wheel-rail materials, F_n represents the normal contact force, d represents the relative wheel-rail sliding distance, H represents

TABLE 1: The values of parameters used in the model.

Parameters		Values	Units
Rails material (nonhardening)	Young's modulus	190	GPa
	Poisson's ratio	0.3	—
	Density	7800	kg/m ³
	Yield stress	610	MPa
	Tangent modulus	19	GPa
	Hardness	360	HV
Wheel material	Young's modulus	210	GPa
	Poisson's ratio	0.3	—
	Density	7800	kg/m ³
	Yield stress	580	MPa
	Tangent modulus	21	GPa
	Hardness	360	HV
Rails material (hardening)	Young's modulus	210	GPa
	Poisson's ratio	0.3	—
	Density	7800	kg/m ³
	Yield stress	2037	MPa
	Tangent modulus	21	GPa
	Hardness	840	HV
Fastening	Vertical	Stiffness	0.35 mN/m
		Damping	40000 Ns/m
Primary suspension	Vertical	Stiffness	2.1 mN/m
		Damping	49000 Ns/m
Axle load		16	t

TABLE 2: Comparison of results from different methods.

Approach	Contact patch			Maximum stress	
	Semiaxis (mm)	Semiaxis (mm)	Area (mm ²)	Vertical (MPa)	Shear (MPa)
Hertz	7.72	5.84	141.6	1090.5	—
CONTACT	7.78	5.71	139.6	1158.4	294.1
FEA	7.81	5.98	146.7	1160.3	296.4
Difference w.r.t. Hertz	-1.15%	-2.34%	-3.48%	-6.02%	—
Difference w.r.t. CONTACT	-0.38%	-4.52%	-4.84%	-0.16%	-0.78%

the material hardness used for wear calculation, and k_w represents the Archard wear coefficient, which can be calculated based on contact stress and the relative sliding velocity at the wheel-rail interface. Figure 9 is drawn based on statistics taken from extensive test results. As can be seen in the figure, the material wear coefficient consists mainly of 4 regions, but since it follows a nonlinear distribution in different regions, it is very difficult to calculate it accurately. To reduce computational complexity, we suppose that the wear coefficient in each region is equal to the midvalue of the wear coefficient interval in this region, namely, $k_1 = k_3 = 5 e^{-4}$, $k_2 = 3.5 e^{-3}$, and $k_4 = 3.5 e^{-2}$. The following is the calculation for the wear depth at unit nodes on the wheel profile:

$$\Delta z = \frac{v_w}{A} = \frac{k_w p d}{H} = \frac{k_w}{H} \sum_{i=1}^n p_i \Delta s_i \Delta T, \quad (5)$$

where p represents the magnitude of contact stress, A represents the wear area of contact patches, and ΔT

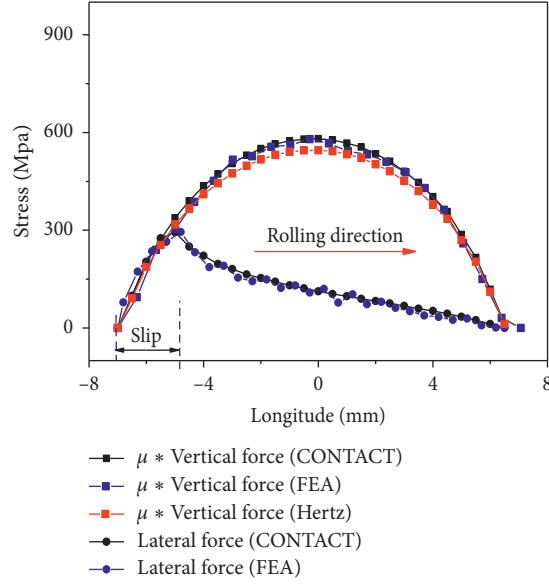


FIGURE 9: Verification of contact results.

represents the time step result output by the FE model (Figure 10) [22].

After the longitudinal wear distribution and depth of the rail is calculated, the wear distribution in the contact patches must be superposed onto the rail profile longitudinally as shown in Figure 11. Typical wear superposition methods fall into either the simplified superposition method or accurate superposition method. And the difference of the maximum wear calculated by the two methods is less than 10% [22]. With calculation accuracy and efficiency taken into full consideration, the simplified superposition method is used to calculate the wear loss of the rail profile.

The simplified superposition method assumes that the parameters such as normal pressure of contact patches, relative wheel-rail slippage, and tangential force remain unchanged, while the wear loss of the rail can be calculated by superimposing it longitudinally on the wear loss of the contact patch at the corresponding position along the line (Figure 8). The simplified superposition formula is as follows:

$$w_D(j) = \sum_{i=1}^{MX} w(i, j), \quad j = 1 - MY, \quad (6)$$

where i and j represent the longitudinal and transversal unit mesh number of the contact patch along the line, MX and MY represent the transversal and longitudinal unit mesh count of the contact patch, $w(i, j)$ represents the wear distribution of the unit mesh numbered (i, j) , and $W_D(j)$ represents the wear loss of the j th unit on the wheel profile when the wheel passes by.

Considering the impact of FE discretization errors and discontinuous system movements in the dynamic simulation process, the measured wheel profile wear follows a zigzag distribution. However, under the impact of the elastoplastic wheel-rail deformation, the plastic deformation distribution and wear curve in wheel-rail contact patches remains

smooth. For higher accuracy of wear prediction, the wear loss needs to be processed by means of a smoothing processing method. So the wheel-rail contact solution and accumulated wear during calculation is smoothen using a linear sliding method. When N data along the overall length are smoothened, different weighted means can be used to characterize smoothening data to inhibit random errors. The expression is as follows:

$$f_k = y_k = \sum_{i=q}^p w_i y_{k+1}, \quad k = q + 1, q + 2, \dots, N - p, \quad (7)$$

where w_i represents the weight coefficient, and $\sum_{i=q}^p w_i = 1$; m represents the amount of data in the smoothing process; p and q represent any integer less than m , and $p + q + m = 1$; and f_j represents a set of N nonstationary data. If m is small and the smoothing effect is low, errors cannot be effectively avoided; when m is large, the smoothing effect is high, but the deterministic components of high-frequency variations may be weakened, meaning a mean rational smoothing parameter is required. After many trials, the smoothing effect was found to be at its best when m is set to 7.

3. Simulation Results for Stress Characteristics

The present section primarily analyzes the effect of surface hardening on the evolution of rolling wheel-rail contact when the wheel rolls along a corrugated rail, which mostly involves evolution of wheel-rail stress/strain and contact force along longitudinal axis of rail. The velocity of the wheel is set to 120 km/h in this simulation process.

Figure 12 shows the evolution of wheel-rail contact force as the wheel runs through hardened and nonhardened corrugated rails. The evolution rule and maximum value of the measured wheel-rail contact force are approximately equal to those described in the literature [14], validating the accuracy of the model. Since the discrete support of the rail

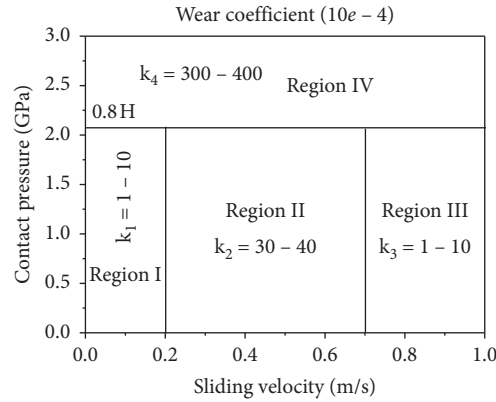


FIGURE 10: Wear coefficient of Archard's model.

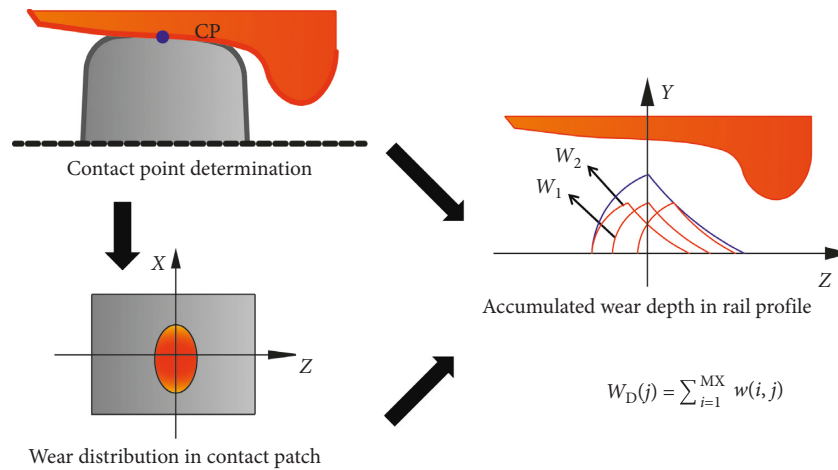


FIGURE 11: Procedure for the simplified wear accumulated method.

fastenings has effect on the dynamic wheel-rail force, the dynamic force near the fastening zone is relatively high. According to the comparison of dynamic force in hardening and nonhardening regions, the maximum contact forces are 133.5 kN (hardening) and 131.8 kN (nonhardening), while the maximum value of the longitudinal wheel-rail forces are 38.6 kN (hardening) and 38.3 kN (nonhardening). After hardening, the wheel-rail vertical force is slightly greater than the nonhardening case. The yield strength and hardness of the rail material increase markedly after hardening, and the quenched zone deforms slightly under wheel loading, while the nonquenched zone deforms far more obviously. This deformation difference causes an increase in vertical irregularities on the rail surface, mildly intensifying the dynamic wheel-rail interaction. When the wheel rolls in an approximately steady state, the longitudinal force is equal to 30% of the wheel load, and when it rolls over the corrugation zone, the longitudinal force is boosted far more obviously than the vertical force.

To explore the impact of surface hardening on the stress characteristics of the rail, an analysis is performed about the stress mechanism on the rail (i.e., when the wheel-rail vertical force reaches its maximum, $t = 0.28$ s). Since contact

stress is primarily related to wheel axle weight, hardening has only a slight effect on the maximum value of the vertical force, meaning there is no need to analyze the impact of hardening on normal contact stress. Therefore, the longitudinal stress, shear stress, and von Mises stress on the rail surface is analyzed:

As shown in Figure 13, hardening has a great impact on the value and distribution of the longitudinal wheel-rail contact stress. Affected by traction force and hardening material, a tensile stress field is generated in front of the contact patch, while a compressive stress field is generated behind the contact patch. In hardening and nonhardening conditions, the maximum tensile stresses on the rail are equal to 161.5 MPa and 157.5 MPa, respectively, while the maximum compressive stresses on the rail are 1305 MPa and 1284 MPa, respectively. As the distribution characteristics of the longitudinal contact stress change, residual compressive stress can only be found inside the nonhardened corrugated rail, while both residual compressive stress and tensile stress zones can be found inside the hardened patch of the corrugated rail. Since the hardening material has a high compressive resistance but low tensile resistance, when the hardening corrugated rail undergoes nonsymmetrical cyclic

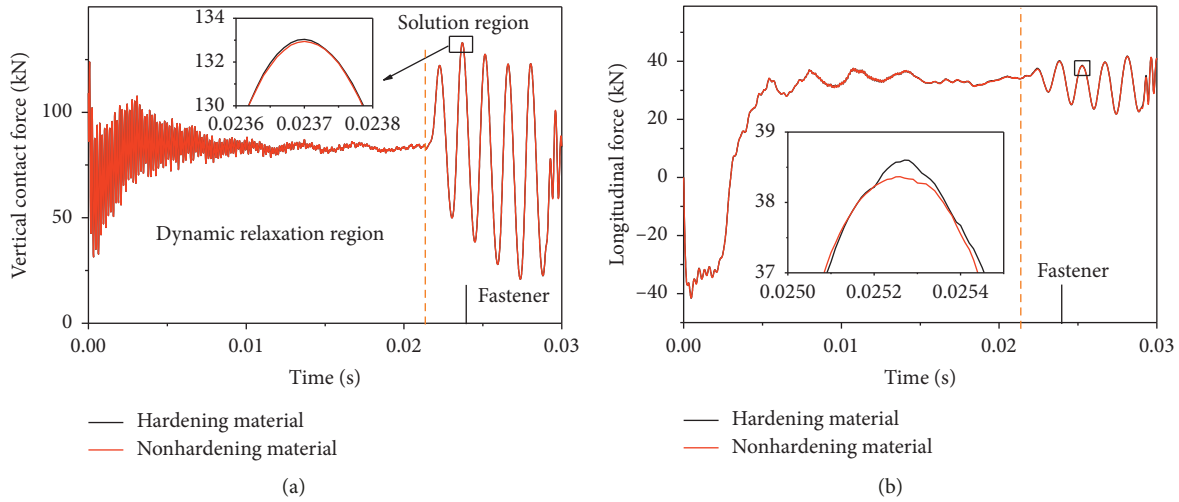


FIGURE 12: Time history curve of contact force: (a) vertical contact force; (b) longitudinal contact force.

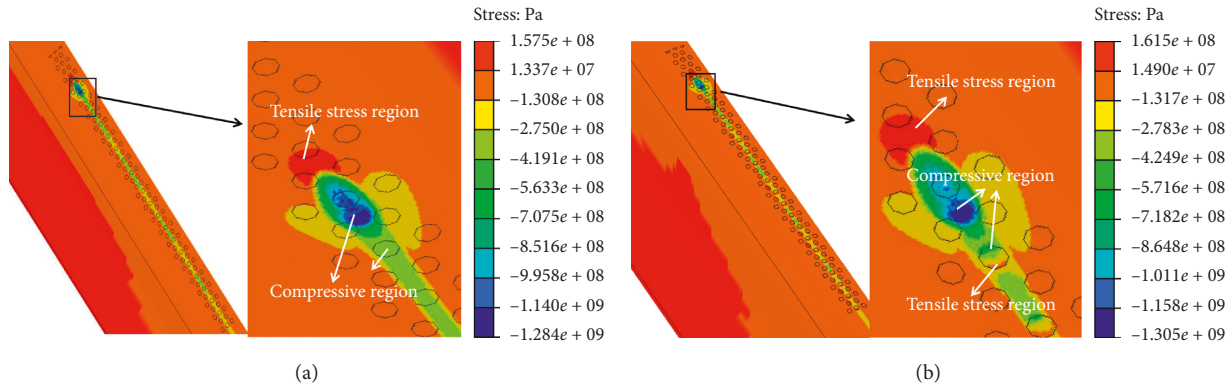


FIGURE 13: Field of longitudinal contact stress on the rail: (a) nonhardening material; (b) hardening material.

tension-compression fatigue loads, the boundary of the hardening patch is susceptible to fatigue, which brings about microcracks.

The field of tangential stress from the xz and yz planes is shown in Figure 14. Both wheel and rail are characterized by bilinear kinematic hardening materials, meaning that, after the wheel rolls through a rail profile, there will be some residual stress left in the rail. If a corrugated rail is not hardened, the xz shear stress on the rail surface is distributed regularly, and there exists no hint of stress concentration. Under these circumstances, there will be some non-symmetric stress effects, whose maximum is 304.3 MPa. On a hardened corrugated rail, some residual stress will be distributed in an irregular fashion, while in the quenched zone, and specifically within 0.5 mm of the boundary of the matrix, there will be an obvious residual stress concentration whose maximum is 390.8 MPa. For the stress in the yz direction, when a corrugated rail is not hardening, stress will be distributed regularly on the surface of the rail, with the maximums of yz shear stress being 482.4 MPa. For a hardening rail, there will be adverse residual stress concentration effects at the boundary of the matrix region and quenched zone within a range of 0.6 mm, with the

maximums of yz shear stress being 619.2 MPa. The percentage changes of xy and yz stresses are 28.4% and 28.3%, respectively. Under the action of nonsymmetric loads, the contact region between quenched and matrix region usually gives rise to crack formation. After hardening, the maximum shear stress in the quenched zone will also be greater than that in the matrix rail. This shows that surface hardening can significantly enhance stress and lead to residual stress concentration effects at the boundary of the quenched zone and matrix region.

The field of von Mises stress is shown in Figure 15. The value and distribution of von Mises stress are susceptible to the hardening technique. Compared with a nonhardened corrugated rail, von Mises stress is concentrated within 0.3 mm of the boundary of the hardening patch on the rail, and the residual von Mises stress after the passage of wheel increases from about 300 MPa to 600 MPa. This shows that surface hardening can significantly increase the residual von Mises stress value. Besides, the maximum von Mises stress is 1241 MPa, while the maximum von Mises of nonhardened rail is 869.3 MPa, indicating that an obvious change of maximum value and distribution takes place. For the reason that the higher the yield limit of a hardening rail material, the

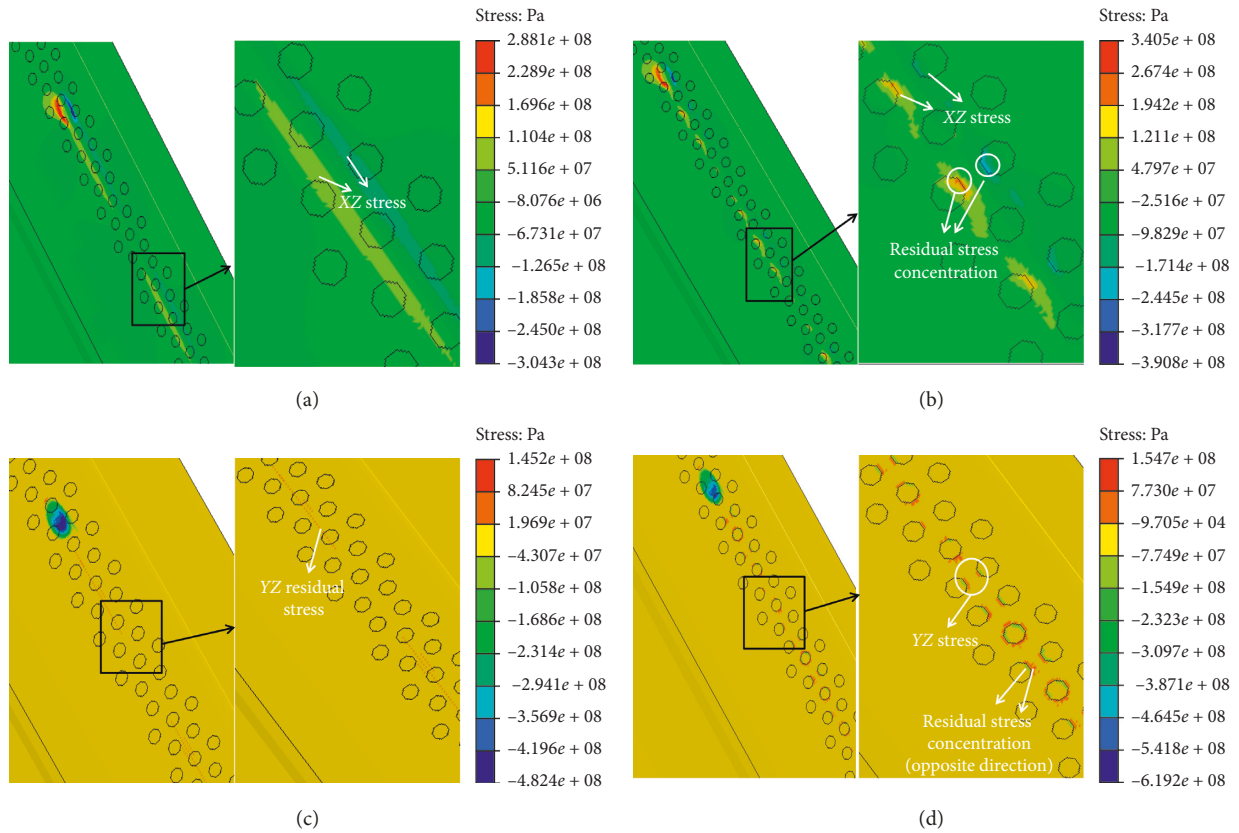


FIGURE 14: Field of shear stress on the rail: (a) xz stress with nonhardening material; (b) xz stress with hardening material; (c) yz stress with nonhardening material; (d) yz stress with hardening material.

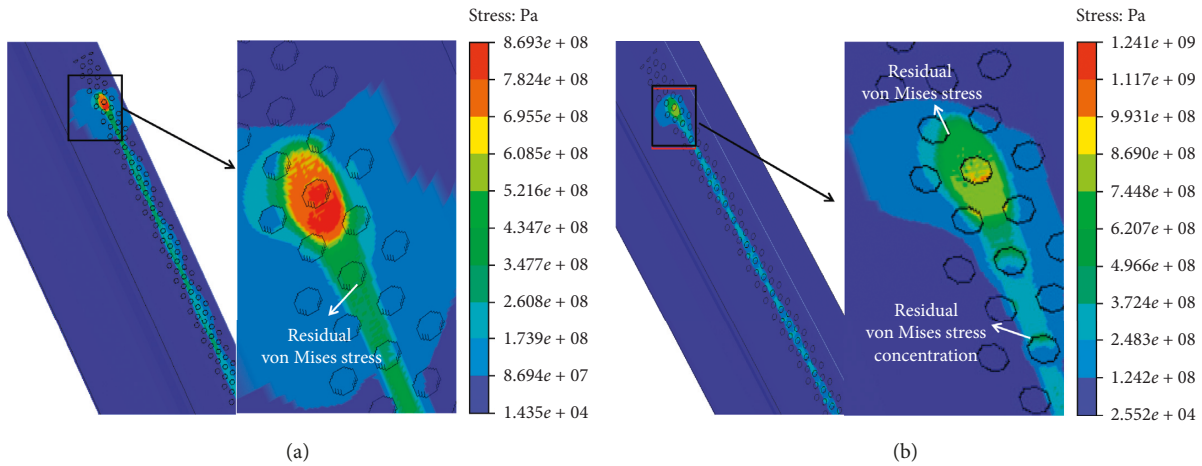


FIGURE 15: Field of von Mises stress on the rail: (a) nonhardening material; (b) hardening material.

more difficult it is for the rail to suffer from a yield effect, the maximum von Mises stress in the rail are increased. In addition, there exists an obvious von Mises stress concentration on the boundary of hardening regions, and due to the impact of torque, stress is primarily concentrated on the front edge of the hardening patch, while the von Mises stress on the rail matrix remains relatively low. Thus, stress peaks are concentrated on the laminar plasma-hardened zone with high yield strength, with the material performance of the

hardened rail fully utilized to enhance the service performance of the rail.

As can be seen in Figure 16, the magnitude and distribution characteristics of axle box acceleration are susceptible to the hardening technique. Before the wheel entering into corrugated rail region, the axle acceleration is relative small, and the value fluctuates between -100 m/s^2 and 100 mm/s^2 . In the corrugation region, the fluctuation of axle acceleration becomes

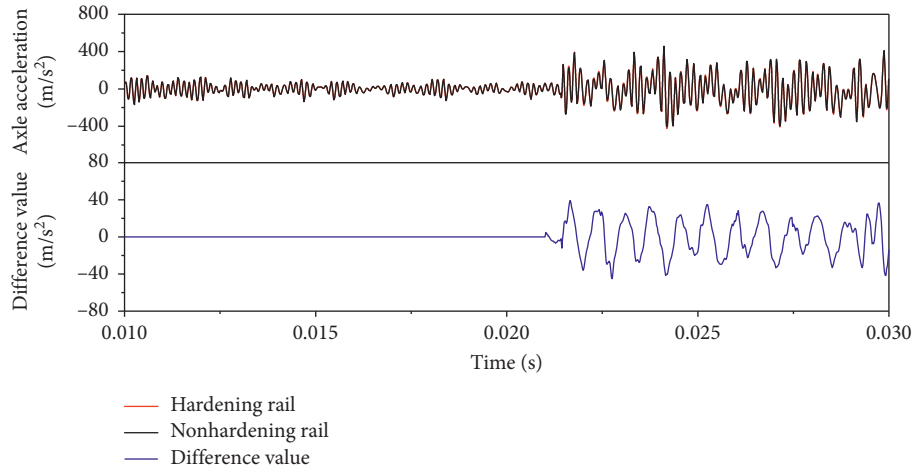


FIGURE 16: Time history curve axle acceleration and difference value between nonhardening material and hardening material.

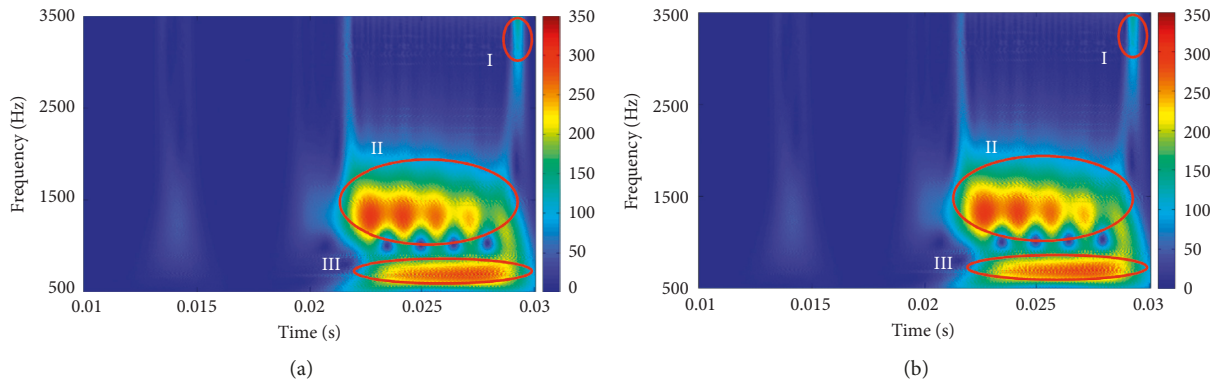


FIGURE 17: Time-frequency distribution spectrogram of axle box acceleration: (a) hardening material; (b) nonhardening material.

violent, it fluctuates between -350 m/s^2 and 350 m/s^2 , and the corrugated rail can significantly increase the vibration of the axle box. Compared to hardening rail, the range of difference value fluctuates between -40 m/s^2 to 40 m/s^2 . Due to the difference of yield strength and hardness between the hardening region and nonhardening region, the differences of plastic deformation will lead to small step at the boundary between hardening and nonhardening regions, and then the step will significantly increase the value of axle acceleration. However, the phase of acceleration is basically unchanged.

As can be seen in Figure 17(a), the time-frequency distribution spectrogram is obtained through wavelet transformation. There exist three typical regions with high energy. The region I is 3000 Hz after the wheel goes through the corrugation region, and it should be ignored. This is due to the larger size of element after the corrugation region. Then, the two regions (II and III) are about 1435 Hz and 642 Hz and mainly appears in the corrugated rail region with high energy. It indicates that the corrugation has great impact on axle vibration acceleration. Compared to nonhardening material, the frequency is almost the same, and only the shades of color indicate higher energy after hardening.

4. Degradation of Rail with Wave Corrugation

To reveal the inhibitory action of surface hardening on metro rail corrugation, this paper tries to explore both plastic strain and wear.

As shown in Figure 18, after surface hardening, an obvious change will take place in the distribution of the shear strain on the corrugated rail surface. For yz strain, the maximum strain is located at the matrix region on the rail surface after hardening. Since the yield strength of the rail material in the quenched zone is relatively high, there is no yz plastic strain generated in this area. For xz strain, obvious strain is mainly located about 0.25 mm beyond the boundary between the quenched zone and the matrix region, while there is no strain generated in the quenched zone. To be more precise, the radius of affected area is 0.25 mm, but there is just a slight change in the overall plastic shear strain value of the rail, while the maximum plastic strain is concentrated in the matrix region with good plastic deformation capacity. As can be seen, surface hardening can enhance the serviceability of rails by taking good advantage of the material performance of the nonhardened rail matrix.

As can be seen in Figure 19, the plastic strain of the rail surface declines substantially under the influence of surface

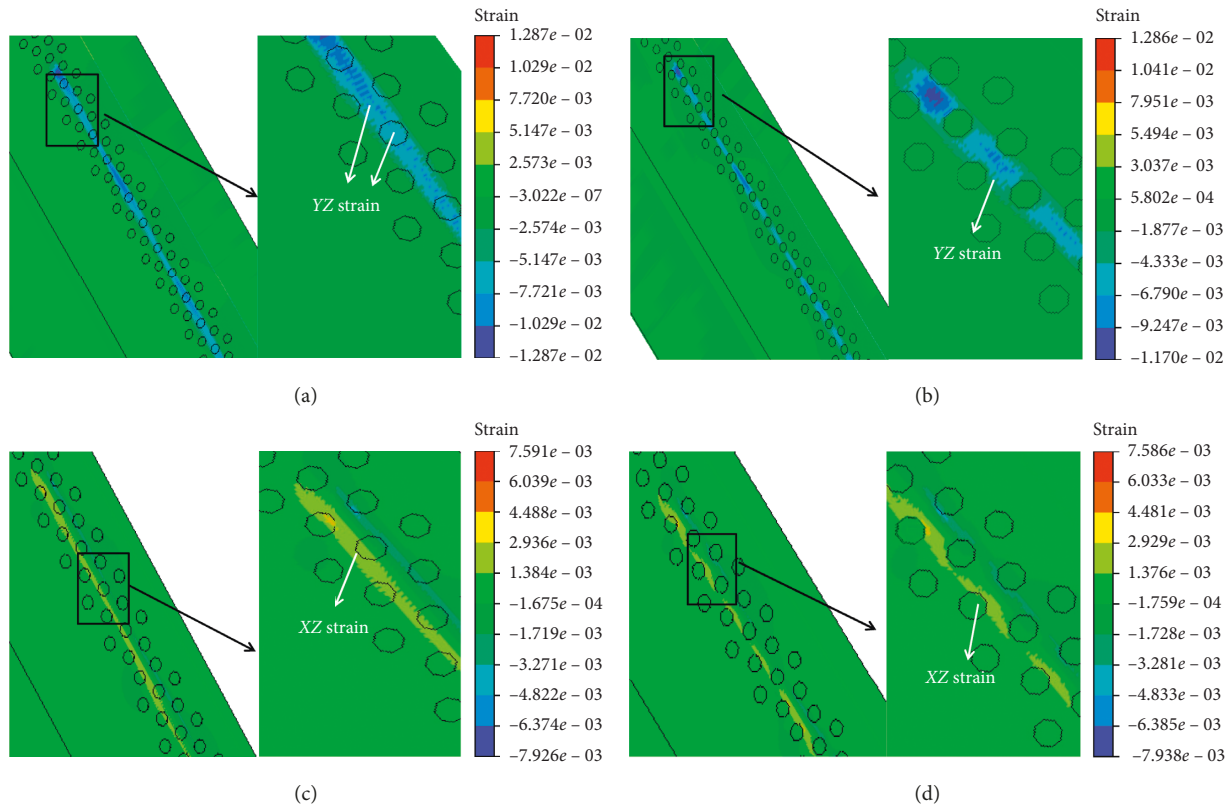


FIGURE 18: Field of shear strain on the rail: (a) yz strain with nonhardening material; (b) yz strain with hardening material; (c) xz strain with nonhardening material; (d) xz strain with hardening material.

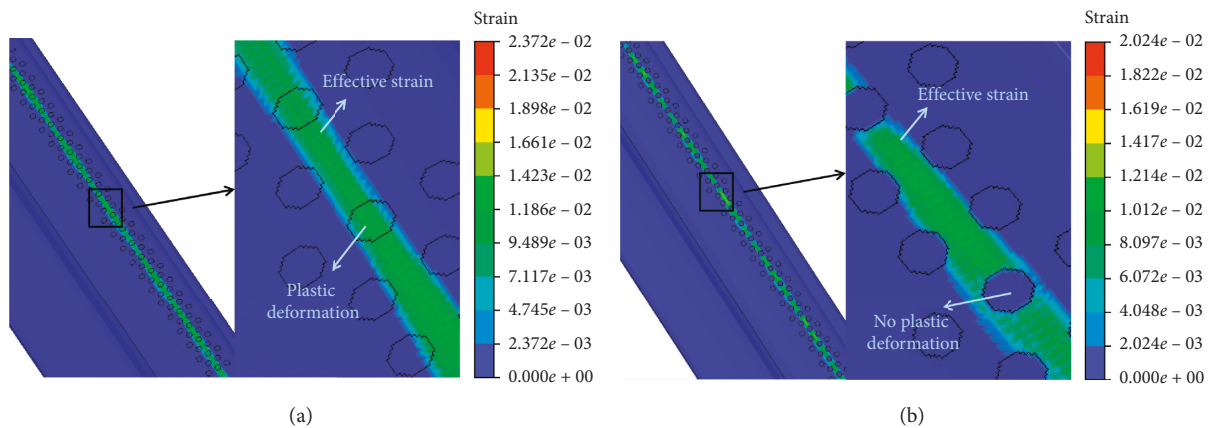


FIGURE 19: Effective field strain on the rail: (a) nonhardening material; (b) hardening material.

hardening. This is because yield strength increases in the quenched zone and improves its plastic strain resistance (Figure 15). For the nonhardened rail, the plastic strain on the rail surface follows a regular distribution under wheel loading, with no sudden change region appearing, and the maximum plastic strain is 0.002024. For the hardening rail, the plastic deformation resistance of its matrix material is lower than the quenched zone, so the plastic strain of the matrix region is relative higher (with maximum strain as high as 0.002372), while the von Mises stress in the quenched zone is lower than the yield strength, meaning no plastic

deformation occurs in this area. This shows that plastic deformation primarily occurs in the matrix region, which is relatively soft compared to hardening regions. The equivalent stress peak mainly acts on the quenched zone. Therefore, surface hardening can cause stress peaks to become concentrated in the quenched zone with higher hardness and yield strength, while plastic strain peaks are concentrated in the matrix region with good plastic deformation capacity; in this way, the material performance of both quenched and nonquenched zones are brought into full play.

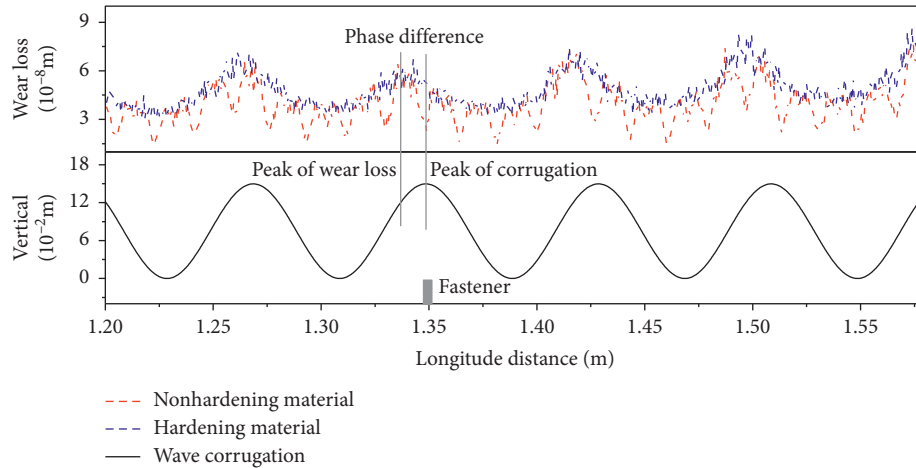


FIGURE 20: Wear loss along longitudinal direction of rail with hardening and nonhardening material.

By effectively combining the transient rolling contact FE model and the Archard wear model as well as the simplified superimposition method, the longitudinal distribution of corrugated rail wear (Figure 20) can be calculated. The maximum rail wear loss does not appear at the crest, the wear peak lies between the crests of rail corrugation, with a phase difference between rail wear and geometric fluctuations in rail corrugation. The wear loss curve of the non-hardened corrugated rail is relatively smooth, and its value is greater than the hardened corrugated rail. For the hardened corrugated rail, due to a significant rise in the yield strength and hardness of the hardening patch, an obvious convex-down area can be observed (a quenched zone) on the wear curve, whose wear loss has declined significantly. The wear depth of material with hardening technology is about 36% of that of material with nonhardening. In addition, the wear loss at the crest is significantly larger than that at the trough, with the rate of wear at the crest being far higher than that at the trough. Wear can be significantly prevented from further deteriorating, suggesting that the surface hardening technique is an effective means for stopping rail corrugation from worsening.

5. Conclusion

In this paper, the geometric feature size of metro rail corrugation was measured by the corrugation inspection car. Based on the measured data, a 3D FE model of the transient rolling contact was established taking into consideration the corrugated rail, and the properties of hardened materials are introduced in the model to analyze the stress mechanism and vibration characteristics of hardening and nonhardening rails under wheel loading. Finally, the wear distribution regularities based on an Archard material model was investigated, leading to the following conclusions:

- (1) The surface hardening technique has little impact on normal contact forces and adhesion distribution characteristics but has a significant impact on the value and distribution of shear stress at the rail

surface, generating obvious tension-compression stress zones before and behind the contact patch.

- (2) The residual von Mises stress is concentrated at the boundary between the quenched zone and the matrix region, making it easy for microcracks to occur in this area; the residual shear stress is concentrated within 0.5 mm of the boundary of the matrix region. Equivalent strain acts on this region, while the most obvious strain fluctuations appear within 0.25 mm at the boundary between the quenched zone and the matrix region.
- (3) The hardening rail will significantly increase the value of axle acceleration in time domain but has little effect on the frequency of axle acceleration in the frequency domain, and the frequency is mainly concentrated in 1435 Hz and 642 Hz.
- (4) The overall shear stress and von Mises stress value of the hardening rail rises, while the plastic shear strain and equivalent strain decline significantly. Moreover, plastic strain is concentrated in the matrix structure, which exhibits a good plastic deformation capacity, while the residual stress peak is concentrated in the quenched zone, which has higher yield strength under wheel loading. The performance of the quenched zone and matrix material is brought into full play.
- (5) After hardening, a phase difference appears between corrugated rail wear and the geometric graph of wear, and the wear loss at the crest is larger than that at the trough. Moreover, the corrugated rail wear loss declines sharply after hardening, suggesting that hardening can significantly prevent rail corrugation from further worsening.

This paper only simulated the stress characteristics of rails under once-through rolling contact conditions using a 3D transient rolling contact FE model. However, after hardening, rail wear also leads to a further change in the wheel-rail contact. Therefore, in the future we will also consider the inhibitory action of hardening on rail corrugation under multiple-rolling contact conditions.

Data Availability

The data used to support the findings of this study are available from the corresponding author upon request.

Conflicts of Interest

The authors declare that they have no conflicts of interest.

Acknowledgments

This study was supported by the National Key Research and Development Program of China (2016YFB1102600), National Natural Science Foundation of China (51608459, 51778542, and U1734207), Fundamental Research Funds for the Central Universities (2682018CX01), Key Research and Development Projects of Science and Technology Program for Sichuan Province (2019YFG0283), and Cultivation Program for the Excellent Doctoral Dissertation of Southwest Jiaotong University.

References

- [1] N. Bosso and N. Zampieri, "Experimental and numerical simulation of wheel-rail adhesion and wear using a scaled roller rig and a real-time contact code," *Shock and Vibration*, vol. 2014, Article ID 385018, 14 pages, 2014.
- [2] K. Wang, W. Zhai, K. Lv, and Z. Chen, "Numerical investigation on wheel-rail dynamic vibration excited by rail spalling in high-speed railway," *Shock and Vibration*, vol. 2016, Article ID 9108780, 11 pages, 2016.
- [3] S. L. Grassie, "Rail corrugation: characteristics, causes, and treatments," *Proceedings of the Institution of Mechanical Engineers, Part F: Journal of Rail and Rapid Transit*, vol. 223, no. 6, pp. 581–596, 2009.
- [4] P. T. Torstensson and M. Schilke, "Rail corrugation growth on small radius curves—measurements and validation of a numerical prediction model," *Wear*, vol. 303, no. 1-2, pp. 381–396, 2013.
- [5] W. J. T. Daniel, R. J. Horwood, P. A. Meehan, and N. Wheatley, "Analysis of rail corrugation in cornering," *Wear*, vol. 265, no. 9-10, pp. 1183–1192, 2008.
- [6] J. C. O. Nielsen, "Numerical prediction of rail roughness growth on tangent railway tracks," *Journal of Sound and Vibration*, vol. 267, no. 3, pp. 537–548, 2003.
- [7] P. Vila, J. Fayos, and L. Baeza, "Simulation of the evolution of rail corrugation using a rotating flexible wheelset model," *Vehicle System Dynamic*, vol. 49, no. 11, pp. 1749–1769, 2011.
- [8] L. Ling, W. Li, H. Shang, X. Xiao, Z. Wen, and X. Jin, "Experimental and numerical investigation of the effect of rail corrugation on the behaviour of rail fastenings," *Vehicle System Dynamics*, vol. 52, no. 9, pp. 1211–1231, 2014.
- [9] X. S. Jin, X. B. Xiao, Z. F. Wen, and Z. G. Zhou, "Effect of sleeper pitch on rail corrugation at a tangent track in vehicle hunting," *Wear*, vol. 265, no. 9-10, pp. 1163–1175, 2008.
- [10] L. Baeza, P. Vila, G. Xie, and S. D. Iwnicki, "Prediction of rail corrugation using a rotating flexible wheelset coupled with a flexible track model and a non-Hertzian/non-steady contact model," *Journal of Sound and Vibration*, vol. 330, no. 18-19, pp. 4493–4507, 2011.
- [11] R. Richard, *In-Track Demonstration of Laser-Treated Rail to Reduce Friction and Wear*, Department of Transportation, Federal Railroad Administration, Office of Research and Development, Washington, DC, USA, 2007.
- [12] Y. Zheng, Q. Hu, C. Li et al., "A novel laser surface compositing by selective laser quenching to enhance railway service life," *Tribology International*, vol. 106, pp. 46–54, 2017.
- [13] X. Cao, L. B. Shi, Z. B. Cai, Q. Y. Liu, Z. R. Zhou, and W. J. Wang, "Investigation on the microstructure and damage characteristics of wheel and rail materials subject to laser dispersed quenching," *Applied Surface Science*, vol. 450, pp. 468–483, 2018.
- [14] D. F. Zeng and L. T. Lu, "Enhancement of rolling contact wear and fatigue resistance of wheel steel by laser dispersed treatment," *Advanced Materials Research*, vol. 891-892, pp. 1797–1802, 2014.
- [15] S. M. Shariff, T. K. Pal, G. Padmanabham, and S. V. Joshi, "Sliding wear behaviour of laser surface modified pearlitic rail steel," *Surface Engineering*, vol. 26, no. 3, pp. 199–208, 2010.
- [16] X. Zhao, Z. Wen, H. Wang, X. Jin, and M. Zhu, "Modeling of high-speed wheel-rail rolling contact on a corrugated rail and corrugation development," *Journal of Zhejiang University Science A*, vol. 15, no. 12, pp. 946–963, 2014.
- [17] S. L. Grassie, "Rail corrugation: advances in measurement, understanding and treatment," *Wear*, vol. 258, no. 3, pp. 1224–1234, 2005.
- [18] Y. Shan, Y. Shu, and S. Zhou, "Finite-infinite element coupled analysis on the influence of material parameters on the dynamic properties of transition zones," *Construction and Building Materials*, vol. 148, pp. 548–558, 2017.
- [19] S.-H. Liu, C.-X. Li, L. Li et al., "Development of long laminar plasma jet on thermal spraying process: microstructures of zirconia coatings," *Surface and Coatings Technology*, vol. 337, pp. 241–249, 2018.
- [20] V. A. Korotkov and M. V. Zlokazov, "Studying wear resistance of carbon steels strengthened by plasma hardening," *Journal of Friction and Wear*, vol. 35, no. 2, pp. 133–136, 2014.
- [21] X. Zhao, X. Zhao, C. Liu, Z. Wen, and X. Jin, "A study on dynamic stress intensity factors of rail cracks at high speeds by a 3D explicit finite element model of rolling contact," *Wear*, vol. 366-367, pp. 60–70, 2016.
- [22] P. Wang, J. Xu, K. Xie, and R. Chen, "Numerical simulation of rail profiles evolution in the switch panel of a railway turnout," *Wear*, vol. 366-367, pp. 105–115, 2016.
- [23] Y. Xiang, D. Yu, F. Liu, C. Lv, and J. Yao, "Determining the heat flux distribution of laminar plasma jet impinging upon a flat surface: an indirect method using surface transformation hardening," *International Journal of Heat and Mass Transfer*, vol. 118, pp. 879–889, 2018.
- [24] W. Hui, Z. Xu, Y. Zhang, X. Zhao, C. Shao, and Y. Weng, "Hydrogen embrittlement behavior of high strength rail steels: a comparison between pearlitic and bainitic microstructures," *Materials Science and Engineering: A*, vol. 704, pp. 199–206, 2017.

